

Neural network based analysis of multimodal bond distributions using extended x-ray absorption fine structure spectra

Nicholas Marcella ^{1,*} Stephen Lam ² Vyacheslav S. Bryantsev,³ Santanu Roy ³ and Anatoly I. Frenkel ^{4,5,†}

¹Department of Chemistry, University of Illinois, Urbana, Illinois 61801, USA

²Department of Chemical Engineering, University of Massachusetts Lowell, Lowell, Massachusetts 01854, USA

³Chemical Sciences Division, Oak Ridge National Laboratory, Oak Ridge, Tennessee 37830, USA

⁴Department of Materials Science and Chemical Engineering, Stony Brook University, Stony Brook, New York 11794, USA

⁵Chemistry Division, Brookhaven National Laboratory, Upton, New York 11973, USA



(Received 10 August 2023; revised 18 January 2024; accepted 7 February 2024; published 1 March 2024)

Knowledge of the local coordination environment around atomic species in functional materials is critical for understanding their mechanisms of operation. Heterogeneous mixtures of metal complexes are ubiquitous in catalysts, ionic liquids, molten salts, biological enzymes, and geochemical systems, among many others. Extracting information from ensemble-average measurements about the structural and compositional descriptors of each type of coordination complex comprising the mixture is not generally possible, especially when they possess multimodal bond-length distributions. We developed a method that enables the mapping of an x-ray absorption spectrum on the radial distribution function describing the average environment of the metal ions. The supervised neural network based method utilizes an objective training set, for which the choice of the local structural motifs is completely agnostic to the theoretically expected structure and dynamics of the modeled system. The method was validated using first-principles modeling of structural dynamics of nickel complexation in molten salts, and it applies to a large class of heterogeneous systems, including those studied under *in situ* and *operando* conditions.

DOI: [10.1103/PhysRevB.109.104201](https://doi.org/10.1103/PhysRevB.109.104201)

I. INTRODUCTION

Investigating the local environment around atomic or ionic species in functional materials helps understand mechanisms of their operation in diverse applications such as nanocatalysts [1], quantum dots [2,3], molten salt systems for nuclear reactors [4], chemical warfare filtration [5], and micro- and nanoactuators [6]. Characterizing atomic distributions in these and other multicomponent and strongly disordered systems poses a major challenge due to the need for elemental specificity, which allows for distinguishing between different neighboring atoms in the same coordination sphere of a given atomic species, and spatiotemporal resolution, which must be sufficient for quantitative analysis of atomic displacements from ensemble-average positions due to static and/or dynamic disorder. Extended x-ray absorption fine structure (EXAFS) is an excellent tool for such purposes due to its excellent elemental specificity and spatiotemporal resolution.

In EXAFS theory, the absorption coefficient of x rays is given by real-space multiple scattering (RSMS) theory, focusing on the interference between the outgoing and backscattered (by nearest neighbors to the absorber) photoelectron waves [7]. The spectrum for an absorber-neighbor

pair is given by

$$\chi(k) = S_0^2 \int_a^b A(k, r) \frac{1}{r^2} \sin[2kr + \delta(k, r)] g(r) dr, \quad (1)$$

where S_0^2 is the passive electron reduction factor, $A(k, r)$ is the photoelectron scattering function that also includes inelastic losses, $\delta(k, r)$ is the photoelectron phase shift, and $g(r)$ is the unknown pair-distribution function of nearest neighbors to x-ray absorbing atoms, which is normalized by the condition $\int_a^b g(r) dr = N$, the number of neighbors to the absorber in the distance range $a < r < b$, corresponding to the given shell. Equation (1) can be modified to include multiple scattering contributions by replacing $g(r)$ with corresponding many-atom distribution functions [8]. Provided a 3D structure, the photoelectron scattering parameters are readily calculated via the Rehr-Albers approach under the muffin-tin approximation of the atomic potentials [9] with the FEFF software package [10]. For well-defined structures, such as those of most bulk materials, EXAFS calculations agree well with experimental spectra [11]. However, in most functional nanomaterials with unknown structure, various methods are used to approximate the needed structural information, in particular the pair-distribution function, $g(r)$.

A typical EXAFS research project often approximates the $g(r)$ as quasi-Gaussian, using a finite (usually, first 3–4 terms) number of terms in the cumulant expansion [12] through nonlinear least-square fitting. This approach notably breaks down in materials with anomalously large, asymmetric bonding disorder [13,14]. “Inverse” methods, such as the “regularization”

*nmarcella@bnl.gov

†frenkel@bnl.gov

[15–24] and “splice” methods [25,26] are very useful techniques for reconstructing a model-independent $g(r)$ in different types of ordered and disordered materials. In the “forward” modeling, $g(r)$ is calculated via molecular dynamics (MD) simulations and validated by matching the EXAFS calculated on MD trajectories (MD-EXAFS) to experimental data [27–30]. Alternative methods like reverse Monte Carlo (RMC) simulations [31,32] rely on assumed initial structures, which are often not known in low-dimensional and/or strongly disordered materials.

Another inverse modeling approach in which the unknown $g(r)$ is obtained from the experimental EXAFS data is by using neural networks (NN-EXAFS) [13]. In the original work developing this method for studying disordered states of Fe during its high-temperature transition from the body-centered cubic to the face-centered-cubic (fcc) phase, and in subsequent applications of this method to the studies of mono- and bimetallic nanoparticles [33,34], Timoshenko, Frenkel, and others trained the feedforward neural network to recognize the relationship between the input (EXAFS spectrum) and the output: $g(r)$. The EXAFS signal, including multiple scattering contributions, is mapped onto one of the pair-distribution functions in this approach. The general concept of the inversion of Eq. (1) and mapping EXAFS data on the $g(r)$ is shown in Fig. 1. In the existing approach for training the NN [Fig. 1(b)], classical MD is used as a practical way to create an array of geometries from which EXAFS spectra are calculated per time step and labeled with the corresponding histogram for the $g(r)$. This approach to structure generation is “subjective” in the sense that the structure is determined by an assumed or *ab initio* interaction potential. MD provides instantaneous 3D structures and $g(r)$, while FEFF calculates EXAFS on those structures. Finally, the NN inverts the input (experimental) spectrum onto $g(r)$, determined by the bond-length histogram. Provided that the MD simulations adequately represent the system of interest, the FEFF-calculated scattering parameters are accurate, and the background subtraction is handled appropriately, the trained NN can be used to invert the experimental data onto $g(r)$.

For many types of material systems, however, the use of MD for generating training sets is impractical. While effective for bulk and nanoscale metals and alloys [35–37], classical MD faces limitations in reactive environments where bonds frequently form or break, such as, e.g., in metal catalysts, transition metals, and actinides in ionic liquids or molten salts [4,38–41]. In these cases, *ab initio* molecular dynamics (AIMD) can model EXAFS spectra in disordered environments, making it useful for constructing NN-EXAFS training sets [4,29,42,43]. However, AIMD is computationally expensive and subject to sampling biases, limiting the generality of NN-EXAFS. The sensitivity of EXAFS to factors like temperature and composition necessitates rerunning AIMD simulations to match experimental conditions. Although machine-learned force fields could reduce costs [44–48], they may still suffer from biases in configurational sampling due to the underlying density-functional theory functionals, which have their own limitations for predicting structural and thermodynamic properties [49].

Ultimately, any of these techniques can be modified on an *ad hoc* basis to provide structures for NN-EXAFS train-

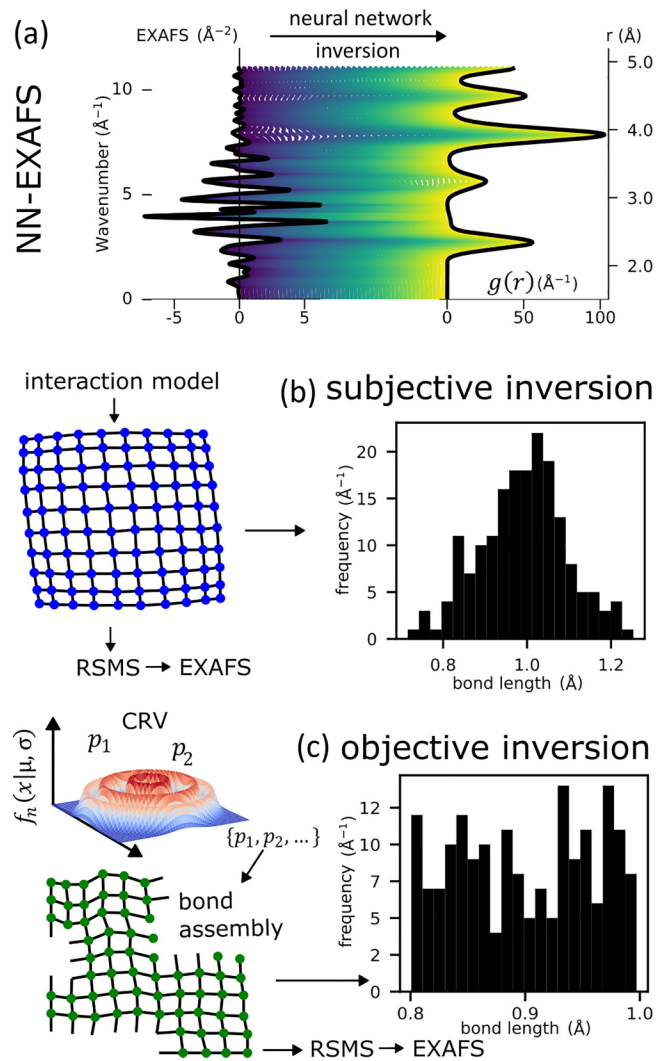


FIG. 1. Schematic of the inversion of an EXAFS spectrum using the subjective (based on MD simulations) and objective (CRV) methods for structure generation. (a) The neural network function maps $\chi(k)$ (left) to $g(r)$ (right), as shown using an example of bulk Ni. (b) Existing training data construction scheme relies on an interaction model embedded in molecular dynamics simulations. Real-space multiple scattering (RSMS) is used to calculate the EXAFS from the structure model. (c) This objective approach uses CRVs for generating pair distances via the probability density function $f(x|\mu, \sigma)$. The macrostate is the user-defined set of CRVs for the overall pair distance distribution. The microstate, or list of pair distances p , is sampled from the macrostate using random variate sampling (RVS). Ultimately, the microstate, or pair distances, will be assembled into a 3D structure model for RSMS calculations.

ing, such as scaling trajectories or varying thermodynamic conditions. However, these modifications increase complexity and limit accessibility for typical EXAFS users. In this work, we acknowledge the fact that the NN does not need to learn the EXAFS– $g(r)$ relationship solely from MD. Since EXAFS depends on the atomic coordinates, any method generating these coordinates realistically can create a training set. This motivates exploring alternatives for training NN-EXAFS

models, aiming for high configurational sampling and low computational costs.

In this paper, we present a method for the “objective” training the NNs used to “invert” the EXAFS spectra onto $g(r)$, resulting in objectively trained NN-EXAFS (ONNE). Rather than employing MD to generate training data, we use an algorithm to create local structures based on a combination of the simple Gaussian functions describing pair distributions. We call this objective structure generation [Fig. 1(c)]. Our method can generate training structures from any combination of bond-length distributions, including partial bond-length distributions from coordination shells beyond the first-nearest neighbors, and thus be used to interpolate the configurational space to an arbitrary degree. Moreover, we can incorporate multimodal bond distributions via objective training, where “multimodal” refers to the different types of bond distributions (unimodal, bimodal etc.) within a given (e.g., cation-anion) coordination shell. Using this approach, and similar to other inversion methods described above, such as regularization method, we obtain the overall distribution “objectively” and forgo the need to learn (or assume) what are the individual species that contribute to the heterogeneous mixture, which is a limitation of forward-modeling methods. We verify the key idea using a toy example of an oscillating dimer and a more complex case of bulk Ni. Finally, we demonstrate this method’s utility and limitations by applying it to reconstructing the $g(r)$ from the *a priori* known (calculated with AIMD) EXAFS spectrum in a heterogeneous environment of Ni^{2+} ions in molten salt.

II. METHODS

We present an algorithm to create diverse 3D structures with user-controlled tolerances for coordination numbers, compositions, and radial distances. Essentially, this method inverts a given pair distribution into a 3D structure. Although the problem is ill posed, leading to multiple structures with equivalent radial distances but random angles, this randomness benefits our aim to generate unique scattering paths over a highly interpolated configurational space.

Bond-length distributions are defined by absorber-neighbor pair lengths per coordination shell and per scatterer type if multiple elements are present, utilizing continuous random variables (CRVs) [Fig. 1(c)]. A CRV for each shell, denoted $(v_{n,e})$, is defined where (n) represents the neighbor shell index and (e) the scattering element. The CRVs, collectively referred to as the “macrostate,” each follow a probability density function given by $f_n(x|\mu, \sigma) = \frac{1}{\sigma\sqrt{2\pi}} \exp(-\frac{(x-\mu)^2}{2\sigma^2})$, and are organized into sets $V_e = \{v_{1,e}, v_{2,e}, \dots\}$, where the set V_e is the macrostate, with adjustable mean (μ_n) and standard deviation (σ_n) . To generate the structures, N_n pair lengths, corresponding to the number of neighbors per shell n , are sampled from each CRV of the macrostate to create one list of absorber-neighbor pairs referred to as the “microstate.” Finally, the pairs from the list are assembled into a 3D structural configuration for scattering calculations with FEFF.

Assembling the microstates into configurations presents a challenge due to the many configurations possible for one microstate. Given that the microstate is the list of radial dis-

tances from the center (absorber) to neighboring atoms, we define a “reasonable” structure as one in which the atoms are placed on spherical shells without getting too close to each other. We utilize a genetic algorithm (GA) to create these 3D structures, employing a customizable fitness function that considers constraints on bond lengths and coordination numbers, and optimizes bond angles. The fitness of 3D configurations is determined by maximizing the minimum pair distance between all atoms. Because we hold the distance to the central atom constant and only modify the angles, this has the effect of keeping atoms separated enough so that they do not overlap in space. The details are in the Supplemental Material [51]. The primary assumptions underpinning the ONNE philosophy are that 1) a NN trained on combinations of microstates generated from Gaussian-distributed macrostates can generalize to more complex macrostates, i.e., a network trained on Gaussian distributions can generalize to multimodal distributions, and 2) that a NN trained on combinations of multimodally distributed microstates can generalize to EXAFS calculated on “physically distributed” structures, i.e., the ONNE-trained NN can make predictions on EXAFS that are calculated on structures that are distributed according to either experimental crystal structure refinement or a potential model. We test these assumptions using two cases: first, the harmonically oscillating dimer (see the Appendix) and second, bulk Ni foil. While the dimer case illustrates the ability to reconstruct a multimodal distribution from the EXAFS-like spectra, the bulk Ni example confirms that NN trained on combinations of multimodally distributed microstates can generalize to EXAFS calculated on realistically distributed structures, i.e., those consistent with either reported crystal structures or plausible models.

III. RESULTS AND DISCUSSION

A. ONNE with Ni foil

We utilize the RMC-EXAFS fitting of Ni foil at 298 K from Ref. [13] [Fig. 2(a), inset (iii)] to provide a realistically distributed example. This structure was derived from the iterative perturbation of a periodic fcc Ni crystal structure until the calculated, ensemble-average EXAFS matched the experimental EXAFS. From this structure we calculate EXAFS and $g_{\text{RMC}}(r)$.

The training data are created by considering a set of four CRVs, $V_{\text{Ni}} = \{v_{1,\text{Ni}}, v_{2,\text{Ni}}, v_{3,\text{Ni}}, \text{ and } v_{4,\text{Ni}}\}$, where μ is varied within 10% around the underlying lattice’s pair length and σ is varied to simulate the temperature-dependent Debye-Waller factor [shown in Fig. 2(a), inset (i)]. Microstates are formed using random variate sampling (RVS) to sample pairs per CRV corresponding to fcc-packed bulk Ni. Finally, for each microstate, one iteration of the GA results in one configuration with an absorber in the middle of four shells of 12, 6, 24, and 12 atoms [Fig. 2(a), inset (ii)]. Running the GA multiple times will result in multiple structures with equivalent radial distances and unique angular placements. Full details of dataset construction, NN training, and code repository are provided in the Supplemental Material, Notes, Methods [51].

A precursory analysis of the RMC-EXAFS and $g_{\text{RMC}}(r)$ ensures that both fall within the training data distribution

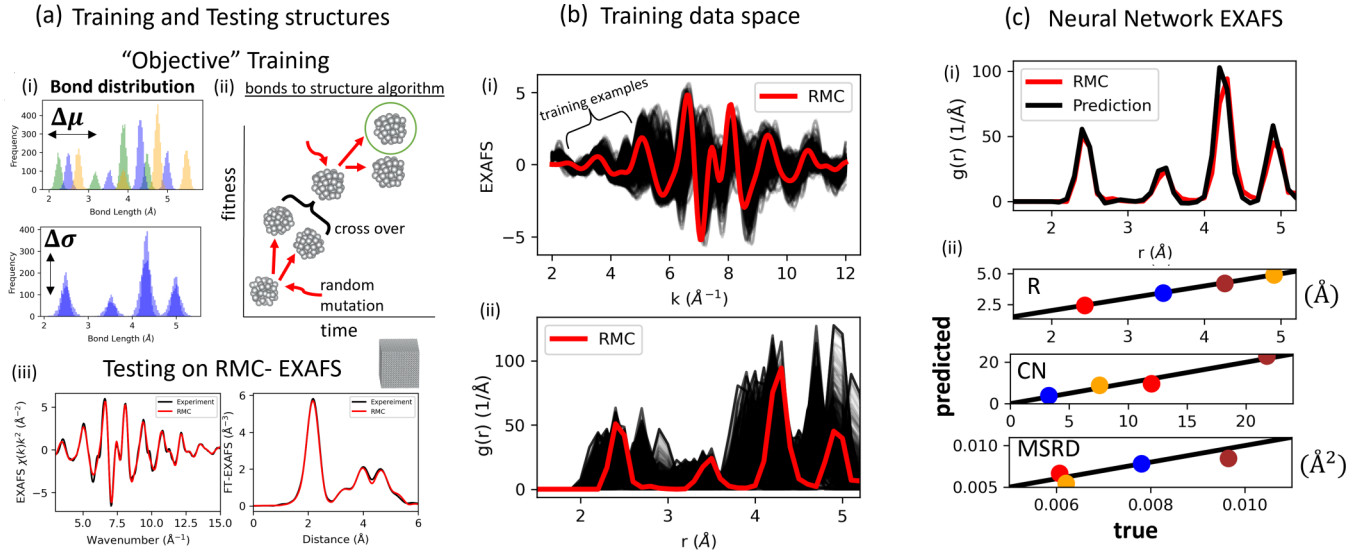


FIG. 2. Deploying the objective training framework for the inversion of the Ni K -edge EXAFS of bulk Ni. (a) Bulk training and testing structures. (a), inset (i): Forty-six macrostates with variations in distribution means (μ) and standard deviations (σ) are created. (a), inset (ii): One hundred microstates are created and assembled into 3D configurations with a genetic algorithm. (a), inset (iii): Existing RMC-EXAFS is used to test the objectively trained neural network. (b) Examples of the training EXAFS (top) and $g(r)$ (bottom) compared to the testing data (red). (c) Top, panel (i) The results of prediction (black) vs true (red) $g(r)$ and (bottom), panel (ii) Agreement between the structural parameters extracted from the predicted and true $g(r)$ for the first (red), second (blue), third (brown), and fourth (yellow) neighbor shells.

[Fig. 2(b)]. The results are shown in Fig. 2(c), where the predicted and true $g_{\text{RMC}}(r)$ are compared. The agreement is excellent in both the visual examination of $g_{\text{RMC}}(r)$ [Fig. 2(b), inset (i)] and the quantitative comparison of interatomic distances (R), coordination numbers (CN), and mean-squared relative displacements per neighbor shell. Therefore, we can conclude that the objectively trained NN can invert physically distributed data despite being trained on nonphysical configurations. The success here is likely due to the appropriateness of the muffin-tin approximation for bulk metals and our ability to highly interpolate this relatively constrained configuration space, i.e., the probability is high that we randomly generated scattering paths that exist in the physically distributed model.

B. ONNE with Ni²⁺ ions in a molten mixture

We examine the system we denote as NiClZnK, consisting of dilute (1 wt.%) NiCl₂ in molten KCl-ZnCl₂ salt mixtures, with two compositions, comp 1 (45.3 mol.% KCl) and comp 2 (52.5 mol.% KCl), previously studied in Ref. [39]. Roy *et al.* used EXAFS and AIMD simulations to capture Ni²⁺ local environments for both compositions. They found that after segmenting the AIMD trajectories into representative Ni complexes by Ni-Cl coordination number and then through linear combination fitting of the EXAFS of those complexes to the experimental spectrum, a match was achieved, resulting in the trust in this physical model and FEFF's ability to simulate EXAFS in this system. Thus, for our testing, their AIMD-EXAFS data will be used, as we know both the spectra and the corresponding $g(r)$.

We define the macrostates using three sets of continuous variables: $V_{\text{Cl}} = \{v_{1,\text{Cl}}, v_{3,\text{Cl}}\}$, $V_{\text{Zn}} = \{v_{2,\text{Zn}}\}$, and $V_{\text{K}} = \{v_{3,\text{K}}\}$, corresponding to their respective shells (Cl, Zn, and Cl/K). The shell composition is varied by changing the coordination

of the first and second shells during RVS (from 1 to 6 for Cl⁻ and 0 to 2 for Zn²⁺). The GA creates configurations [Fig. 3(a)], and the NN is trained using weighted linear combinations with an on-the-fly synthetic data generator. The convolutional NN, full details of dataset construction, NN training, and code repository are provided in the Supplemental Material, Notes, Methods [51].

The ONNE results for both compositions are shown in the left column of Fig. 3(b), where the partial distributions $g_{\text{Cl}}(r)$ and $g_{\text{Zn}}(r)$ from AIMD-EXAFS are compared to the true distributions from the AIMD trajectories. We trained ten separate NNs for uncertainty assessment, displaying average predictions (solid lines) and standard deviations (green shadow). Qualitative agreement is observed, such as the bimodality and skewness of $g_{\text{Zn}}(r)$ in comp 1 and comp 2, but it only permits coarse conclusions about the material's local structure. Average coordination number comparison reveals 26 and 15% errors for comp 1, and 18 and 40% for comp 2, comparable to conventional EXAFS analysis errors (up to 20%). Moreover, consistent systematic changes in CN are noted between comp 1 (predicted: $\text{CN}_{\text{Ni-Cl}} = 3.18 \pm 0.08$ and $\text{CN}_{\text{Ni-Zn}} = 2.13 \pm 0.07$, vs true: $\text{CN}_{\text{Ni-Cl}} = 4.01$ and $\text{CN}_{\text{Ni-Zn}} = 2.51$) and comp 2 (predicted: $\text{CN}_{\text{Ni-Cl}} = 3.11 \pm 0.07$ and $\text{CN}_{\text{Ni-Zn}} = 2.34 \pm 0.09$, vs true: $\text{CN}_{\text{Ni-Cl}} = 3.68$ and $\text{CN}_{\text{Ni-Zn}} = 1.66$). Although gaining information about the second shell [$g_{\text{Zn}}(r)$] is an advantage over the current state of the art, we aim to improve ONNE to enhance the resolution of information from the EXAFS in these systems. Upon further investigation (presented in Supplemental Material, Fig. S2 [51]), we determined that the source of the error stems from an incomplete sampling of the configuration space, which is very large for a system of this complexity. Thus, in the future development of ONNE, we need to develop a more robust protocol for interpolating the configurational space.

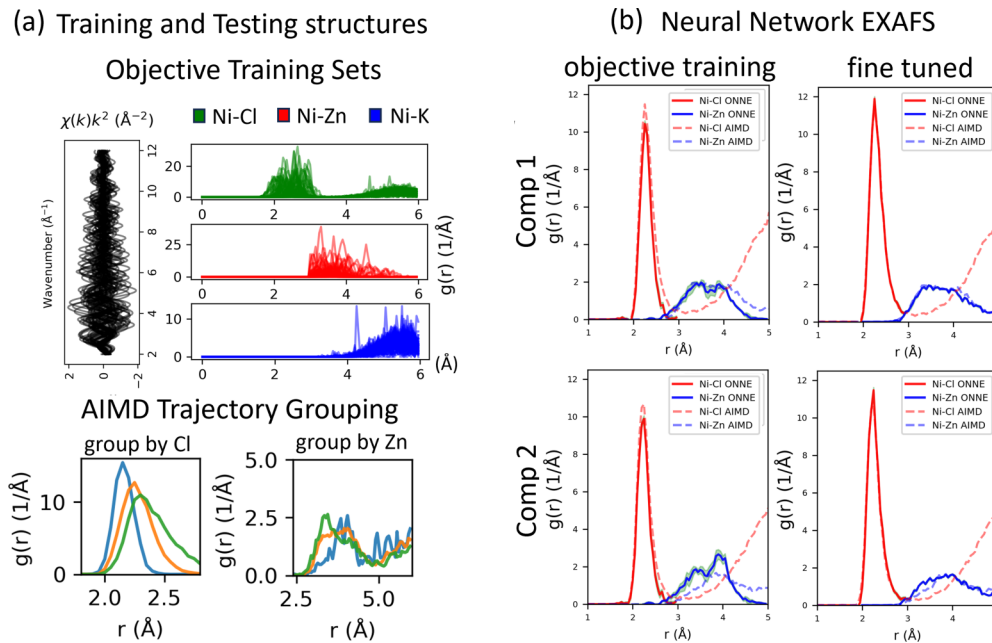


FIG. 3. Objective training and fine-tuning NN-EXAFS for NiClZnK Ni K -edge EXAFS spectra inversion. (a) The objective training sets and AIMD test data. (b) Objectively trained Neural Network EXAFS (ONNE) predictions (left column) of the partial Ni-Cl and Ni-Zn $g(r)$ for AIMD-simulated NiClZnK of comp 1 (top row) and comp 2 (bottom row) at 550 °C. ONNE is compared to fine-tuning (right column), where the data from composition 1 were used to fine-tune.

C. Fine-tuning ONNE

In the final part, we demonstrate how ONNE can be “fine-tuned” using the available AIMD simulations. Since ONNE is already trained and has learned the general relationship between EXAFS and partial $g_{\text{Cl}}(r)$ and $g_{\text{Zn}}(r)$, we employ a transfer learning [50] procedure called fine-tuning to enhance the model for immediate use in our research. Fine-tuning augments a pretrained NN with more layers, freezing the previous ones (Supplemental Material, Fig. S1 [51]). This method is effective if the pretrained NN’s data domain is similar to these data, which is true here. It is important to note that the use of AIMD data in this context is optional, serving primarily to refine the model’s precision for specific scenarios and is not a fundamental aspect of the training process. Care must be taken not to overfit the model to this smaller dataset. Fine-tuning can be further refined by using enhanced sampling methods beyond AIMD, such as machine learning based molecular dynamics or temperature-accelerated dynamics. Two fine-tuning datasets were created from AIMD for training and testing to ensure the NN did not memorize the training data.

The AIMD datasets were constructed by grouping trajectories based on the Ni-Cl and Ni-Zn distribution centers, yielding 86 unique configuration averages, 26 examples of which were reserved for validation, with the remaining 60 for training. The ten previously trained NNs are fine-tuned using the on-the-fly synthetic data generator approach, with full details in the Supplemental Material [51].

The fine-tuning results for comp 1 and 2 [Fig. 3(b), right] outperform the original ONNE, and the generalization to comp 2 is promising. Though a more robust ONNE training process may achieve similar outcomes, this offers a signifi-

cant improvement “hack” for this system and an approach to training NN-EXAFS models when MD or AIMD availability is limited.

D. Application to experimental data

ONNE and fine-tuned ONNE (ONNEF) were used to invert the experimental NiClZnK data from Ref. [39] and the results are presented in Fig. S3 in the Supplemental Material [51]. We have obtained the partial Ni-Cl (first shell) and Ni-Zn (second shell) radial distribution functions from the NiClZnK system, which is remarkable when considering that there is no second-shell information seen in the Fourier-transformed EXAFS (FT-EXAFS) data in Fig. S3. The qualitative differences between comp 1 and comp 2 seen in the first shell are in excellent agreement with the FT-EXAFS for both ONNE and ONNEF. The trends in the second shell cannot be distinguished using ONNE, as expected from the validation testing with the AIMD data, but they are distinct using ONNEF.

IV. SUMMARY

We have demonstrated that the training of NN-EXAFS models does not require AIMD (or, indeed, any MD) simulations to generate the training set. Instead, the NN can learn the underlying relationship between photoelectron scattering and the bond-length distribution over which it scatters from arbitrary examples generated by our algorithm. The caveat is that the configurational space over which the examples are generated must be fully sampled. This method of training the NN is objective because it is model independent—i.e., agnostic to any interaction model for the purpose of the 3D

structure generation for real-space scattering calculations. In the simple case of bulk Ni, ONNE performs very well due to the limited configurational space. For the more complex NiClZnK molten salt system, ONNE's predictions are less accurate due to the insufficient sampling. Transfer learning can be employed to fine-tune ONNE, enabling structural analysis of the next coordination shells via NN-EXAFS. Future efforts will focus on enhancing ONNE by developing a more robust method for sampling in systems with greater configurational complexity.

The digital data for all figures, tables, charts, and any other media contained in this paper and its associated supporting information files will be made accessible on the Zenodo repository [55].

ACKNOWLEDGMENTS

This work was primarily supported as part of the Molten Salts in Extreme Environments Energy Frontier Research Center, funded by the U.S. Department of Energy (DOE) Office of Science. Brookhaven National Laboratory (BNL) and Oak Ridge National Laboratory are operated under DOE Contracts No. DE-SC0012704 and No. DE-AC05-00OR22725, respectively. N.M. acknowledges support by the U.S. DOE, Office of Basic Energy Sciences Award No. DE-SC0022199. S.L. acknowledges support by the U.S. DOE, Nuclear Energy University Program (NEUP) Award No. DE-NE0009204. The FEFF simulations used resources of the Center for Functional Nanomaterials, which is a U.S. DOE Office of Science Facility, and the Scientific Data and Computing Center, a component of the Computational Science Initiative, at BNL under Contract No. DE-SC0012704. We thank Professor J. J. Rehr for useful discussions.

APPENDIX: THE TOY EXAMPLE OF AN OSCILLATING DIMER

We begin with the toy example investigating a pair of atoms in a harmonically oscillating dimer with the simplified form of Eq. (1) that we used for creating the “toy” spectrum:

$$\chi_t(k, r) = \int_a^b \frac{1}{r^2} \sin[2kr]g(r)dr. \quad (\text{A1})$$

Due to the omission of the amplitude factor and photoelectron scattering functions—see the more general Eq. (1)—this demonstration can be easily generalized to any other test $g(r)$ functions using a sample code (see Supplemental Material, Notes) [51]. In the toy example, we can work with the macrostates directly since we remove the need for scattering calculations, and thus we use the following implementation (for the full details of dataset construction, neural network training, and code repository, see Supplemental Material [51]). The macrostates are created by utilizing RVS of 1000 numbers (pair lengths) from $f_1(x|\mu, \sigma)$ for a range of different μ and σ . The macrostates are binned according to the r -space grid and normalized by Δr , resulting in

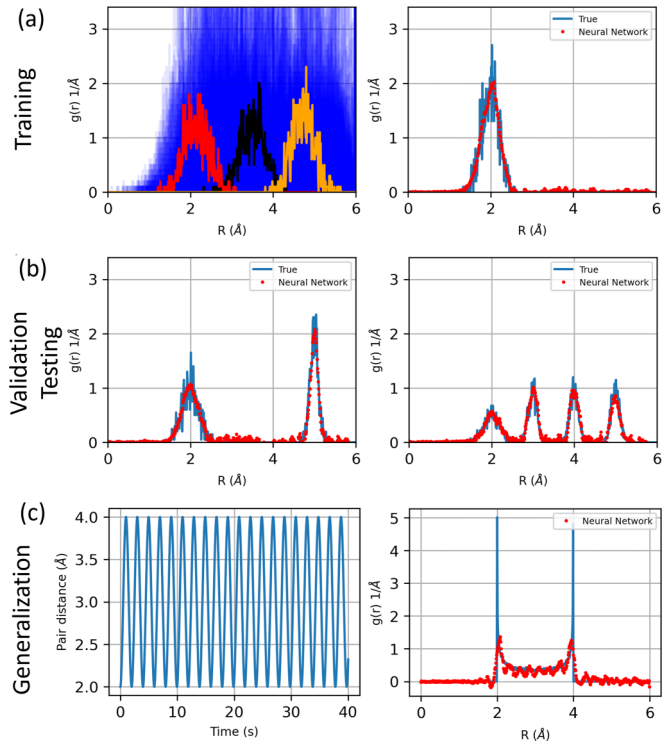


FIG. 4. (a) Left: Examples of the training data distribution with three random examples highlighted (red, black, and orange). Right: One instance of the trained NN prediction vs true $g_t(r)$. (b) Examples of the validation and testing data in which the trained NN predicts on $\chi_t(k)$ created from non-Gaussian $g_t(r)$. (c) A demonstration of the generalization power of the trained NN. (Left) A dimer bond-length distribution is simulated numerically as a harmonic oscillator. (Right) The results of the trained NN prediction on $\chi_t(k)$ created from the harmonic oscillator.

the training distribution function $g_t(r) = \frac{N}{\sigma\sqrt{2\pi}} \exp[-\frac{(r-r_0)^2}{2\sigma^2}]$, which is normalized by the condition: $\int_a^b g(r)dr = N$, where N is the number of neighbors to the absorber in the distance range $a < r < b$ (e.g., $N = 1$ for a dimer). Equation (2) is used to calculate χ_t over a grid of uniform k space from 0 to 12 \AA^{-1} . A basic multilayer perceptron NN was trained on 10 000 macrostates. The results are given in Fig. 4, where the training [Fig. 4(a)], and validation (testing) data [Fig. 4(b)] are compared in terms of true vs predicted $g_t(r)$. In a test of generality, we find that the NN, which was trained to invert χ_t calculated on Gaussian $g(r)$, does an excellent job of predicting $g_t(r)$ from χ_t calculated on asymmetric and multimodal distributions. As a final test, we demonstrated its applicability to an extreme case of a non-Gaussian $g_t(r)$, that of a harmonic oscillator, in which the $g_t(r)$ can be calculated analytically (see Supplemental Material [51]). The excellent agreement confirms that a NN trained on combinations of Gaussian-distributed macrostates can generalize to more complex macrostates [Fig. 4(c)]. This implies that NN-EXAFS learns a general relationship between the EXAFS signal and the pair-distribution function, more general than the underlying shape of the training data.

- [1] Y. Li and A. I. Frenkel, Deciphering the local environment of single-atom catalysts with X-ray absorption spectroscopy, *Acc. Chem. Res.* **54**, 2660 (2021).
- [2] L. Asor, J. Liu, Y. Ossia, D. C. Tripathi, N. Tessler, A. I. Frenkel, and U. Banin, InAs nanocrystals with robust p-type doping, *Adv. Funct. Mater.* **31**, 2007456 (2021).
- [3] J. Liu, Y. Amit, Y. Li, A. M. Plonka, S. Ghose, L. Zhang, E. A. Stach, U. Banin, and A. I. Frenkel, Reversed nanoscale Kirkendall effect in Au–InAs hybrid nanoparticles, *Chem. Mater.* **28**, 8032 (2016).
- [4] S. K. Gill, J. Huang, J. Mausz, R. Gakharm, S. Roy, F. Vila, M. Tropsakal, W. C. Phillips, B. Layne, S. Mahurin *et al.*, Connections between the speciation and solubility of Ni(II) and Co(II) in molten $ZnCl_2$, *J. Phys. Chem. B* **124**, 1253 (2020).
- [5] A. M. Plonka, Q. Wang, W. O. Gordon, A. Balboa, D. Troya, W. Guo, C. H. Sharp, S. D. Senanayake, J. R. Morris, C. L. Hill *et al.*, In situ probes of capture and decomposition of chemical warfare agent simulants by Zr-based metal organic frameworks, *J. Am. Chem. Soc.* **139**, 599 (2017).
- [6] E. Makagon, E. Wachtel, L. Houben, S. R. Cohen, Y. Li, J. Li, A. I. Frenkel, and I. Lubomirsky, All-solid-state electro-chemo-mechanical actuator operating at room temperature, *Adv. Funct. Mater.* **31**, 2006712 (2021).
- [7] J. J. Rehr and R. C. Albers, Theoretical approaches to X-ray absorption fine structure, *Rev. Mod. Phys.* **72**, 621 (2000).
- [8] A. Filipponi, A. Di Cicco, and C. R. Natoli, X-ray-absorption spectroscopy and n-body distribution functions in condensed matter. I. Theory, *Phys. Rev. B* **52**, 15122 (1995).
- [9] J. J. Rehr and R. C. Albers, Scattering-matrix formulation of curved-wave multiple-scattering theory: Application to X-ray-absorption fine structure, *Phys. Rev. B* **41**, 8139 (1990).
- [10] J. Kas, F. Vila, C. Pemmaraju, T. Tan, and J. Rehr, Advanced calculations of X-ray spectroscopies with FEFF10 and Corvus, *J. Synchrotron Radiat.* **28**, 1801 (2021).
- [11] J. J. Rehr, R. C. Albers, and S. I. Zabinsky, Scattering-matrix formulation of curved-wave multiple-scattering theory: Application to x-ray-absorption fine structure, *Phys. Rev. Lett.* **69**, 3397 (1992).
- [12] G. Bunker, Application of the ratio method of EXAFS analysis to disordered systems, *Nucl. Instrum. Methods Phys. Res.* **207**, 437 (1983).
- [13] J. Timoshenko, A. Anspoks, A. Cintins, A. Kuzmin, J. Purans, and A. I. Frenkel, Neural network approach for characterizing structural transformations by X-ray absorption fine structure spectroscopy, *Phys. Rev. Lett.* **120**, 225502 (2018).
- [14] A. Yevick and A. I. Frenkel, Effects of surface disorder on EXAFS modeling of metallic clusters, *Phys. Rev. B* **81**, 115451 (2010).
- [15] N. V. Ershov, A. L. Ageev, V. V. Vasin, and Y. A. Babanov, A new interpretation of EXAFS spectra in real space: II. A comparison of the regularization technique with the Fourier transformation method, *Phys. Status Solidi B* **108**, 103 (1981).
- [16] D. S. Yang and G. Bunker, Improved R-space resolution of EXAFS spectra using combined regularization methods and nonlinear least-squares fitting, *Phys. Rev. B* **54**, 3169 (1996).
- [17] G. Khelashvili and G. Bunker, Practical regularization methods for analysis of EXAFS spectra, *J. Synchrotron Radiat.* **6**, 271 (1999).
- [18] A. Kuzmin and J. Purans, Dehydration of the molybdenum trioxide hydrates $MoO_3 \cdot nH_2O$: In situ X-ray absorption spectroscopy study at the Mo K edge, *J. Phys.: Condens. Matter* **12**, 1959 (2000).
- [19] A. Kuzmin and J. Purans, Local atomic and electronic structure of tungsten ions in AWO_4 crystals of scheelite and wolframite types, *Radiat. Meas.* **33**, 583 (2001).
- [20] M. Kunicke, I. Y. Kamensky, Y. A. Babanov, and H. Funke, Efficient determination of optimal regularization parameter for inverse problem in EXAFS spectroscopy, *Phys. Scr.* **T115**, 237 (2005).
- [21] Y. A. Babanov, Y. A. Salamatov, I. Y. Kamensky, A. V. Ryazhkin, and V. V. Ustinov, Efficient determination of optimal regularization parameter for inverse problem in EXAFS spectroscopy, *J. Electron Spectrosc. Relat. Phenom.* **175**, 27 (2009).
- [22] Y. A. Babanov, D. A. Ponomarev, V. V. Ustinov, A. N. Baranov, and Y. V. Zubavichus, Local atomic structure of solid solutions with overlapping shells by EXAFS: The regularization method, *J. Electron Spectrosc. Relat. Phenom.* **211**, 1 (2016).
- [23] I. Jonane, A. Cintins, A. Kalinko, R. Chernikov, and A. Kuzmin, Probing the thermochromic phase transition in $CuMoO_4$ by EXAFS spectroscopy, *Phys. Status Solidi B* **255**, 1800074 (2018).
- [24] Y. A. Babanov, V. V. Vasin, D. A. Ponomarev, D. I. Devyaterikov, L. N. Romashev, and V. V. Ustinov, Atomic structure of multilayered low-contrast Fe/Cr thin films: Mathematical formalism and numerical experiments, *Phys. Met. Metallogr.* **120**, 756 (2019).
- [25] E. A. Stern, Y. Ma, O. Hanske-Petitpierre, and C. E. Bouldin, Radial distribution function in X-ray-absorption fine structure, *Phys. Rev. B* **46**, 687 (1992).
- [26] A. Frenkel, E. A. Stern, A. Voronel, A. Rubshtein, Y. Ben-Ezra, and V. Fleurov, Redistribution of La-Al nearest-neighbor distances in the metallic glass $Al_{0.91}La_{0.09}$, *Phys. Rev. B* **54**, 884 (1996).
- [27] A. Kuzmin and R. A. Evarestov, Quantum mechanics–molecular dynamics approach to the interpretation of X-ray absorption spectra, *J. Phys.: Condens. Matter.* **21**, 055401 (2009).
- [28] F. Vila, J. J. Rehr, J. Kas, R. G. Nuzzo, and A. I. Frenkel, Dynamic structure in supported Pt nanoclusters: Real-time density functional theory and X-ray spectroscopy simulations, *Phys. Rev. B* **78**, 121404(R) (2008).
- [29] B. J. Palmer, D. M. Pfund, and J. L. Fulton, Direct modeling of EXAFS spectra from molecular dynamics simulations, *J. Phys. Chem.* **100**, 13393 (1996).
- [30] S. W. T. Price, N. Zonias, C.-K. Skylaris, T. I. Hyde, B. Ravel, and A. E. Russell, Fitting EXAFS data using molecular dynamics outputs and a histogram approach, *Phys. Rev. B* **85**, 075439 (2012).
- [31] J. Timoshenko and A. I. Frenkel, Probing structural relaxation in nanosized catalysts by combining EXAFS and reverse Monte Carlo methods, *Catal. Today* **280**, 274 (2017).
- [32] R. L. McGreevy and L. Pusztai, Reverse Monte Carlo simulation: A new technique for the determination of disordered structures, *Mol. Simul.* **1**, 359 (1988).
- [33] J. Timoshenko, C. J. Wrasman, M. Luneau, T. Shirman, M. Cargnello, S. R. Bare, J. Aizenberg, C. M. Friend, and A. I. Frenkel, Probing atomic distributions in mono- and bimetallic nanoparticles by supervised machine learning, *Nano Lett.* **19**, 520 (2019).

- [34] M. Rüscher, A. Herzog, J. Timoshenko, H. S. Jeon, W. Frandsen, S. Kühn, and B. Roldan Cuenya, Tracking heterogeneous structural motifs and the redox behaviour of copper–zinc nanocatalysts for the electrocatalytic CO₂ reduction using operando time resolved spectroscopy and machine learning, *Catal. Sci. Technol.* **12**, 3028 (2022).
- [35] P. D’Angelo, A. Di Nola, M. Mangoni, and N. V. Pavel, An extended x-ray absorption fine structure study by employing molecular dynamics simulations: Bromide ion in methanolic solution, *J. Chem. Phys.* **104**, 1779 (1996).
- [36] A. Anspoks and A. Kuzmin, Interpretation of the Ni K-edge EXAFS in nanocrystalline nickel oxide using molecular dynamics simulations, *J. Non-Cryst. Solids* **357**, 2604 (2011).
- [37] J. Timoshenko, Z. Duan, G. Henkelman, R. M. Crooks, and A. I. Frenkel, Solving the structure and dynamics of metal nanoparticles by combining X-ray absorption fine structure spectroscopy and atomistic structure simulations, *Annual Rev. Anal. Chem.* **12**, 501 (2019).
- [38] S. T. Chill, R. M. Anderson, D. F. Yancey, A. I. Frenkel, R. M. Crooks, and G. Henkelman, Probing the limits of conventional extended x-ray absorption fine structure analysis using thiolated gold nanoparticles, *ACS Nano* **9**, 4036 (2015).
- [39] S. Roy, Y. Liu, M. Topsakal, E. Dias, R. Gakhar, W. C. Phillips, J. F. Wishart, D. Leshchev, P. Halstenberg, S. Dai *et al.*, A holistic approach for elucidating local structure, dynamics, and speciation in molten salts with high structural disorder, *J. Am. Chem. Soc.* **143**, 15298 (2021).
- [40] E. T. Dias, S. K. Gill, Y. Liu, P. Halstenberg, S. Dai, J. Huang, J. Mausz, R. Gakhar, W. C. Phillips, S. Mahurin *et al.*, Radiation-assisted formation of metal nanoparticles in molten salts, *J. Phys. Chem. Lett.* **12**, 157 (2021).
- [41] X. Liu, A. Ronne, L. Yu, Y. Liu, M. Ge, C. Lin, B. Layne, P. Halstenberg, D. S. Maltsev, A. S. Ivanov *et al.*, Formation of three-dimensional bicontinuous structures via molten salt dealloying studied in real-time by in situ synchrotron X-ray nano-tomography, *Nat. Commun.* **12**, 3441 (2021).
- [42] P. Liu, V. Johansson, H. Trilaksana, J. Rosdahl, G. G. Andersson, and L. Kloo, EXAFS, ab initio molecular dynamics, and NICIS spectroscopy studies on an organic dye model at the dye-sensitized solar cell photoelectrode interface, *ACS Appl. Mater. Interfaces* **9**, 19773 (2017).
- [43] R. Atta-Fynn, E. J. Bylaska, G. K. Schenter, and W. A. de Jong, EXAFS, ab initio molecular dynamics, and NICIS spectroscopy studies on an organic dye model at the dye-sensitized solar cell photoelectrode interface, *J. Phys. Chem. A* **115**, 4665 (2011).
- [44] D. P. Kovács, C. van der Oord, J. Kucera, A. E. Allen, D. J. Cole, C. Ortner, and G. Csányi, Linear atomic cluster expansion force fields for organic molecules: Beyond RMSE, *J. Chem. Theory Comput.* **17**, 7696 (2021).
- [45] S. Batzner, A. Musaelian, L. Sun, M. Geiger, J. P. Mailoa, M. Kornbluth, N. Molinari, T. E. Smidt, and B. Kozinsky, Linear atomic cluster expansion force fields for organic molecules: Beyond rmse, *Nat. Commun.* **13**, 2453 (2022).
- [46] A. Musaelian, S. Batzner, A. Johansson, L. Sun, C. J. Owen, M. Kornbluth, and B. Kozinsky, Learning local equivariant representations for large-scale atomistic dynamics, *Nat. Commun.* **14**, 579 (2023).
- [47] C. J. Owen, S. B. Torrisi, Y. Xie, S. Batzner, J. Coulter, A. Musaelian, L. Sun, and B. Kozinsky, Complexity of many-body interactions in transition metals via machine-learned force fields from the TM23 data set, [arXiv:2302.12993](https://arxiv.org/abs/2302.12993).
- [48] J. Vandermause, Y. Xie, J. S. Lim, C. J. Owen, and B. Kozinsky, Active learning of reactive Bayesian force fields applied to heterogeneous catalysis dynamics of H/Pt, *Nat. Commun.* **13**, 5183 (2022).
- [49] C. J. Owen, N. Marcella, Y. Xie, J. Vandermause, A. I. Frenkel, R. G. Nuzzo, and B. Kozinsky, Unraveling the catalytic effect of hydrogen adsorption on Pt nanoparticle shape-change, [arXiv:2306.00901](https://arxiv.org/abs/2306.00901).
- [50] C. Tan, F. Sun, T. Kong, W. Zhang, C. Yang, and C. Liu, A survey on deep transfer learning, in *Artificial Neural Networks and Machine Learning – ICANN 2018*, edited by V. Kůrková *et al.* (Springer International Publishing, Cham, 2018), p. 270.
- [51] See Supplemental Material at <http://link.aps.org/supplemental/10.1103/PhysRevB.109.104201> for the link to our code repository, technical details of GA and NN implementation, and figures with further analysis of the training data with respect to Ni-Zn radius, which includes Refs. [52–54].
- [52] F.-A. Fortin, F.-M. De Rainville, M.-A. G. Gardner, M. Parizeau, and C. Gagné, DEAP: Evolutionary algorithms made easy, *J. Mach. Learn. Res.* **13**, 2171 (2012).
- [53] R. Swinbank and R. James Purser, Fibonacci grids: A novel approach to global modelling, *Q. J. R. Meteorol. Soc.* **132**, 1769 (2006).
- [54] P. Gavrikov, [visualkeras](https://github.com/pavlovskiy/visualkeras), [GitHub repository](https://github.com/pavlovskiy/visualkeras) (2020).
- [55] See the Zenodo repository under doi: [10.5281/zenodo.8279733](https://doi.org/10.5281/zenodo.8279733).